Carbohydrate Polymer Technologies and Applications 9 (2025) 100710

Contents lists available at ScienceDirect

Carbohydrate Polymer Technologies and Applications

journal homepage: www.sciencedirect.com/journal/carbohydrate-polymer-technologies-and-applications

Amorphous calcium phosphate reinforced alginate-dialdehyde-gelatin (ADA-GEL) bioink for biofabrication of bone tissue scaffolds

Abhishek Indurkar [a,b], Susanne Heid [c], Julian Bauer [d,e], Kristaps Rubenis [a,b], Oliver Friedrich [d,e], Janis Locs [a,b], Aldo R. Boccaccini [c,*]

[a] Institute of Biomaterials and Bioengineering, Faculty of Natural Sciences and Technology, Riga Technical University, Riga, Pulka 3, LV-1007, Latvia
[b] Baltic Biomaterials Centre of Excellence, Headquarters at Riga Technical University, Kipsalas Street 6A, Riga LV-1048, Latvia
[c] Institute of Biomaterials, Department of Material Science and Engineering, Friedrich-Alexander University Erlangen-Nürnberg, Cauerstraße 6, Erlangen 91058, Germany
[d] Institute of Medical Biotechnology, Friedrich-Alexander University Erlangen-Nürnberg, Paul-Gordan-Str. 3, Erlangen 91052, Germany
[e] Erlangen Graduate School in Advanced Optical Technologies (SAOT), Friedrich-Alexander University Erlangen-Nürnberg, Erlangen 91052, Germany

ARTICLE INFO

Keywords:
Citrate stabilized amorphous calcium phosphate
Alginate dialdehyde-gelatin bioink
Nanocomposite bioink
Bioprinting
Bone tissue engineering

ABSTRACT

The aim of this work was to develop a nanocomposite bioink closely resembling the nanostructure of bone incorporating amorphous calcium phosphate (ACP) as an inorganic counterpart, specifically, citrate stabilized ACP (ACP_CIT) and non-stabilized ACP (ACP_ACE) in an organic hydrogel matrix consisted of alginate dialdehyde-gelatin (ADA-GEL). The hydrogel's physical properties were evaluated, confirming the reinforcement effect of ACP. The frequency sweep analysis showed that G' and G" of ADA-GEL were 99 ± 9 Pa and 9 ± 1 Pa, respectively. By the addition of ACP_ACE, G' and G" increased. Overall, the viscoelastic and mechanical properties of ADA-GEL hydrogel were enhanced by ACP. ACP_CIT was more effective than ACP_ACE. Further, printing parameters were optimized. The bioink was formulated by embedding MC3T3-E1 cells in ADA-GEL and ACP-reinforced ADA-GEL hydrogels, followed by fabricating scaffolds at optimized printing parameters (pressure: 65 kPa, speed: 5 mm/s). Crosslinking was performed by immersing constructs in $CaCl_2$ and microbial transglutaminase solution. Post-printing analysis was performed using the printability index and average pore area analysis. The lowest structural stability was observed in ADA-GEL constructs. The highest structural stability was noted in ADA-GEL-ACP_CIT constructs. Epifluorescence and two-photon microscopy of Rhodamine/Phalloidin stained constructs confirmed the cytocompatibility of the bioinks.

1. Introduction

Scaffold development for tissue engineering has evolved significantly, with various fabrication techniques tailored to mimic the complexity of the natural extracellular matrix (Negrini et al., 2021). Conventional methods such as electrospinning, freeze drying and solvent casting have been widely used for developing scaffolds with high porosity and surface area (Suamte et al., 2023). For instance, electrospinning offers excellent control over fiber morphology, enabling creation of nanofibrous scaffolds (Ghorbani et al., 2023). On the other hand, freeze drying excels in producing porous scaffolds with interconnected network (Liu et al., 2024), while solvent casting is effective in the fabrication of films and membranes (Joseph et al., 2023). However, these fabrication techniques are incapable of precisely controlling pore size, pore geometry, spatial distribution of pores, construction of inner channels within the scaffold, replicating complex geometries and homogenous distribution of cells within the scaffold (Kundu et al., 2014). In contrast, bioprinting represents a transformative layer-by-layer approach to scaffold fabrication which allows precise deposition of biomaterials and cells (Duarte Campos et al., 2019). The ability to tailor structure and compositional properties at the microscale imparts bioprinting substantial advantages over conventional scaffold fabrication techniques (Vanaei et al., 2021).

Bioprinting has shown significant capacity in fabricating complex and hierarchically organized constructs with architecture closely resembling bone (Kim et al., 2020). The printable material, called bioink, is a combination of cells and hydrogel, a crucial component of bioprinting (Li et al., 2021). The biosynthesis of the inorganic component (calcium phosphate, bioactive glass) and its association with the organic counterpart must be considered to develop biomimetic

---

* Corresponding author.
E-mail address: aldo.boccaccini@fau.de (A.R. Boccaccini).

https://doi.org/10.1016/j.carpta.2025.100710

nanocomposite bioinks (Indurkar et al., 2023a). Amorphous calcium phosphate (ACP) is the first inorganic phase synthesized and stabilized in the mitochondria of cells. Further, ACP is embedded in the 40 nm gap zone of the collagen matrix, where it crystallizes to apatite (Ap) (Indurkar et al., 2023a; Lehninger, 1970). Bone repair and reconstruction require innovative strategies that account for the nano to macro-scale hierarchical assembly of tissue (Zhu et al., 2020). Therefore, we have developed a nanocomposite bioink reinforced with ACP in the current study.

Despite being the first calcium phosphate phase synthesized by cells, the application of ACP has been relatively limited in tissue engineering compared to other calcium phosphates. In literature, ACP has been utilized to make nanocomposites, but the stabilization of ACP was not considered (Buschmann et al., 2012; Chen et al., 2015; Cheng, Weir, Xu, Antonucci, Kraigsley, et al., 2012; Cheng, Weir, Xu, Antonucci, Lin, et al., 2012; Hou et al., 2022; Hwang et al., 2013; Jiang et al., 2021; Niu et al., 2017; Sun et al., 2019; Weir et al., 2012; Wolint et al., 2021; Xu et al., 2011). The stabilizing agent is essential in regulating collagen interfibrillar mineralization (Liu et al., 2011; Nudelman et al., 2013). Various materials have been utilized to stabilize ACP by surface adsorption or ion substitution. Typical, organic compounds stabilizing ACP by surface adsorption are adenosine triphosphate (ATP), polyelectrolyte, citrate, and polyethylene glycol (Chen et al., 2014; Krogstad et al., 2014; Schweikle et al., 2019a). Moreover, magnesium, zinc, iron, carbonates, pyrophosphates, and fluorine ions can stabilize ACP by substituting calcium or phosphate ions (Chen et al., 2023; Jin et al., 2018; Schweikle et al., 2019b). Citrate is a favorable stabilizing agent as it is naturally synthesized through the Krebs cycle in mitochondria which are also a site for ACP synthesis (Williams & O'Neill, 2018). Recent findings revealed that one-sixth of the available surface area of Ap is covered by citrate, and NMR analysis also confirmed its presence in the bone (Hu et al., 2010; Xie & Nancollas, 2010). Moreover, it has the inherent property of osteo-inductivity and enhances collagen mineralization through interface wetting (Costello et al., 2012; Granchi et al., 2019; Shao et al., 2018).

Gelatin (GEL) and alginate dialdehyde (ADA) were used as organic counterparts of the nanocomposite bioink. GEL is a single-stranded protein obtained from the hydrolytic degradation of collagen. It consists of glycine, proline, and hydroxyproline residues that display similar biomechanical properties to collagen (Fukunishi et al., 2017). Alginate is a natural polymer obtained from brown seaweed consisting of β-(1–4) linked to d-mannuronic acid and β-(1–4) linked with I-glucuronic acid units. It lacks a cell attachment site and is often used with GEL to fabricate 3D scaffolds (Łabowska et al., 2021). Alginate lacks binding properties with GEL; therefore, it is commonly modified to alginate dialdehyde (ADA), offering reactive groups for crosslinking with GEL by Schiff base formation, thus forming ADA-GEL (Heid et al., 2022).

Several nanocomposite bioinks have been formulated for bone tissue regeneration (Yu & Wei, 2021). Most nanocomposite bioinks include Ap, tricalcium phosphate (TCP), octacalcium phosphate (OCP) or bioactive glasses as inorganic counterparts (Bozo et al., 2020; Jeong et al., 2019). ACP is the first naturally synthesized calcium phosphate phase, but it has not yet been considered in bioink formulations. Therefore, in this study we have utilized ACP variants for developing a nanocomposite bioink which presents a promising option to fabricate resorbable scaffolds for bone tissue engineering (BTE) applications. In our previous study, we analyzed the transformation of ACP to Ap in the presence of various small organic molecules. The results revealed that acetate rapidly transformed ACP to Ap, whereas citrate was the slowest (Indurkar et al., 2023c). Therefore, we have utilized citrate and acetate-containing ACP in this study to develop a new nanocomposite bioink. To evaluate the effect of slow (ACP_CIT) and fast (ACP_ACE) transforming ACP on ADA-GEL physiochemical properties, two nanocomposite bioinks were investigated and pure ADA-GEL was used as a control. The bioinks were developed by embedding MC3T3-E1 cells, and cell-laden constructs were fabricated. Subsequently, preprinting and post-printing analyses were performed to evaluate the suitability of the new bioinks for bioprinting applications. ADA-GEL-ACP bioinks have the potential to serve as bioresorbable materials for applications in bone tissue engineering.

2. Materials and methods

Calcium acetate monohydrate was procured from Honeywell, Fluka, USA (CAS 114,460–21–8). Calcium citrate tetrahydrate (CAS 5785–44–4), trisodium phosphate (CAS 7601–54–9), sodium hydroxide (CAS 1301–73–2), and gelatin type-A from porcine skin (CAS 9000–70–8) were procured from Sigma Aldrich, Germany. Ethylene glycol (CAS 107–21–1) was obtained from VWR Chemical International (USA). Sodium meta periodate (CAS 7790–28–5) was procured from Bioultra, ≥ 99.5, Sigma Aldrich, Germany. Sodium alginate (CAS 9005–38–3) was obtained from VIVAPHARM®, JSR Pharma GmbH & Co, KG Rosenberg, Germany. The dialysis membrane with molecular cut-off 6–8 kDa was obtained from Spectrum lab™, USA.

2.1. Synthesis of ACP

ACP was synthesized using the protocol described in a previous publication (Indurkar et al., 2023b). Briefly, for the synthesis of ACP_CIT, 50 mM of calcium citrate tetrahydrate was added into Milli-Q® water. Moreover, for the synthesis of ACP_ACE, 150 mM calcium acetate was added to Milli-Q® water. The pH of the calcium citrate and calcium acetate solutions was adjusted to 11.5 using 3 M NaOH. Further, 100 mM of trisodium phosphate solution was rapidly added (in 1:1 ratio) to the beakers containing ACP_CIT and ACP_ACE solution. The precipitate was isolated by centrifugation and washed thrice with Milli-Q® water. The precipitates were frozen in liquid nitrogen, followed by lyophilization for 72 h. The obtained powder was used for characterization and bioink formulation.

2.2. Synthesis of ADA

According to a slightly modified protocol presented by Sarker et al., ADA was prepared by oxidation of sodium alginate (Sarker et al., 2017). Briefly, 10 g of sodium alginate was dispersed in 50 ml ethanol, and 2.67 g of sodium metaperiodate was dissolved in 50 ml of Milli-Q® water. An equal amount of sodium metaperiodate was added dropwise in the 50 ml sodium alginate dispersion under constant stirring. The reaction was performed in the dark. Further, the reaction was quenched after six hours by adding 10 ml ethylene glycol to deactivate excess periodate ions, and the mixing continued for another 30 min. The mixtures were then collected into 50 ml Falcon tubes and centrifuged at 2500 rpm for 5 min, and then the ethanol phase was decanted. The remaining ADA solution was dialyzed in Milli-Q® water for four days and replenished daily. The product was removed from the dialysis membrane, transferred to a clean tray, and it was frozen for at least 24 h before lyophilization (Christ Alpha, 1–4LD, Christ Gefriertrocknungsanlangen, Osterode am Harz, Germany). Subsequently the final dry product was harvested.

2.3. Chemical characterization

2.3.1. X-ray powder diffraction (XRD)

XRD analysis was performed to examine the phases of ACP_ACE and ACP_CIT using a PANalytical Aeris diffractometer (The Netherlands). The diffraction data were collected at 40 kV and 15 mA in a step mode with a step size of 0.04°, in the 2θ range from 10 to 70°.

2.3.2. Field-emission gun transmission electron microscopy (FEG-TEM)

The morphology and particle size of ACP_ACE and ACP_CIT were evaluated by FEG-TEM (FEI, Tecnai G2 F30, USA) operated at 300 kV. The sample preparation was as follows: a small amount of powder was dispersed in isopropyl alcohol and sonicated in an ultrasonic bath.

Further, the samples were placed on a carbon-coated grid and dried before analysis.

2.3.3. Fourier-transformed infrared spectroscopy (FTIR)

FTIR analysis was performed to analyze the functional groups in ACP. Furthermore, FTIR analysis investigated ADA modification and the Schiff-base formation in ADA-GEL. Samples were analyzed in transmission mode from the wavenumber ranging from 4000 to 400 cm^{-1} with a resolution of 4 cm^{-1} (64 scans) using an iS50 FT-IR spectrometer (Thermo Scientific Nicolet Waltham, MA, USA).

2.3.4. Moisture content

The ACP_CIT and ACP_ACE were synthesized according to Section 2.1. The freshly obtained precipitate was analyzed using Kern MRS 120–3 for moisture content.

2.4. Hydrogel precursor solution

To prepare ADA-GEL bioink, 5 % (w/v) GEL solution was prepared in Milli-Q® water at 37 °C and filtered through 0.22 µm Millipore filters (Rotilab-syringe filter, PVDF Carl Roth). 5 % (w/v) ADA solution was prepared in Dulbecco's phosphate buffer saline (DPBS) at 37 °C and filtered through 0.45 µm Millipore filters (Rotilab-syringe filter, PVDF Carl Roth). The solutions of ADA and GEL were filtered only when sterile working conditions were required; otherwise, unfiltered solutions were used.

The following procedure was used to synthesize ACP-reinforced ADA-GEL hydrogels. Initially, sterile synthesis of ACP was performed in which 150 mM calcium acetate, 100 mM trisodium phosphate, and 3 M NaOH solutions were filtered through 0.22 µm Millipore filters. Moreover, 50 mM of calcium citrate was autoclaved at 121 °C at 15 psi for 30 min. The procedure mentioned in Section 2.1 performed ACP synthesis under sterile conditions. Sterile ACP was only synthesized when such working conditions were required.

For hydrogel synthesis, 2 % (w/v) ACP was added to 5 % (w/v) ADA solution and stirred for 5 min until a homogeneous suspension was formed. Further, 5 % (w/v) GEL solution was added in a 1:1 ratio and allowed to stir for 10 min at 37 °C for Schiff's base formation. The mixing of the hydrogels was meticulously performed using positive displacement pipette to ensure uniform and consistent distribution of the components, while effectively preventing formation of air pockets or other structural inconsistencies. The same procedure was utilized for both ACP_CIT and ACP_ACE. ADA-GEL hydrogel was used as a control to allow for comparison with ACP-reinforced ADA-GEL hydrogels. The final composition of the formulated hydrogel was: 2.5 % (w/v) ADA, 2.5 % (w/v) GEL, and 1 % (w/v) ACP.

2.5. Oscillatory shear tests

The printability of hydrogels is regulated by the viscoelastic properties of the material that must be adjusted to create a construct with long-term shape fidelity. Every material has unique viscoelastic properties; for instance, GEL has weak mechanical strength and cannot be used independently in bioprinting (Indurkar et al., 2020; Mao et al., 2020). Therefore, ADA was used in this study to impart mechanical strength. Moreover, ACP was incorporated in ADA-GEL to develop a nanocomposite bioink.

When a new bioink is developed, the oscillator shear test of the hydrogel is first carried out to study its viscoelastic behavior. The tests were performed using an HR20 rheometer (TA Instruments, New Castle, USA) with a 25 mm diameter parallel plate for analysis. Initially, the linear viscoelastic region (LVE) was analyzed using an amplitude sweep performed under a constant frequency of 1 Hz and shear stress ranging from 0.1 to 100 %.

Hydrogels are divided into several categories according to their rheological properties, i.e., Newtonian, shear thinning, and shear thickening fluids (Rehm & Haghshenas, 2012). In the context of 3D bioprinting, shear thinning is an essential property of the hydrogels that determines the resolution, printing pattern, and shape fidelity by preventing shear stress, clogging, and cellular damage (Rehm & Haghshenas, 2012; Wu et al., 2020). Viscosity was measured at a shear rate of 0.1 to 10 s^{-1} to analyze the flow behavior of ADA-GEL and ACP-reinforced ADA-GEL hydrogels. To analyze the effect of ACP on the viscoelastic properties of ADA-GEL hydrogel, frequency sweep analysis was performed under frequencies ranging from 0.1 to 10 Hz to analyze loss modulus (G") and storage modulus (G').

2.6. Compression test

A materials testing device (AllroundLine 20 kN, ZwickRoell GmbH and Co. KG, Germany), equipped with a 100 N load cell and stainless-steel compression plate of 30 mm diameter, was used to determine the maximum tolerable force of the hydrogel by uniaxial compression test. The hydrogel samples were prepared as per the procedure illustrated in Section 2.4. The prepared hydrogel casted into a cylindrical shape with a diameter of 16 mm and a height of 13 mm. The hydrogel sample was placed on the device's bottom plate, and the measurement started at a gap of 13 mm. The top plate with the load cell was moved down at a speed of 1 mm/s. The measurement gap at the load of 0.001 N was defined as the cylinder height. The maximum achievable compression force before the sample rupture (F_{max}) was determined.

2.7. Water uptake capacity

The water uptake capacity was tested using a gravimetric procedure. Initially, the weight of dry samples was recorded (W_0). Subsequently, the dry samples were immersed in 20 ml Milli-Q® water. The scaffold was removed at different time points up to 720 min. The excess water from the scaffold was removed using moist filter paper and the weight was recorded (W_1). The samples' water uptake capacity ($W\%$) was calculated using Eq. (1):

$$W\% = \left(\frac{W_1 - W_0}{W_0}\right) * 100 \tag{1}$$

2.8. Printing optimization

Once the bioink was formulated, printing conditions were optimized for maximum resolution and repeatability. A sequential optimization approach was utilized to optimize printing pressure by keeping a constant printing speed of 2 mm/s. The printing pressure resulting in intact struts and pores was selected. Afterward, the printing speed was adjusted at the constant optimized pressure. The construct was printed at different printing speeds to obtain square-shaped pores. The printing optimization was performed using uncross-linked ADA-GEL hydrogel. A small 8×8 mm^2 dimension construct was printed to avoid wasting the biomaterials and was further analyzed using a stereo microscope (Carl Zeiss, Jena, Germany). This test was performed to assess optimum printing conditions for ADA-GEL hydrogels visually. The optimized printing parameters were further utilized to fabricate the ADA-GEL and ACP-reinforced ADA-GEL constructs.

2.9. Cell printing process

2.9.1. Cell culture

An osteoblast precursor cell line derived from mouse (*Mus musculus*) calvaria (MC3T3-E1, Sigma Aldrich, Germany) was employed for cellular analysis after ten passages. MC3T3-E1 cells were maintained in an α-MEM medium containing 10 vol% Fetal bovine serum (FBS; Sigma Aldrich, Germany) and 10 vol% penicillin-streptomycin at 37 °C in a humidified atmosphere of 95 % air and 5 % CO_2. The cultures of MC3T3-E1 cells were trypsinized by adding 3 ml of trypsin-EDTA solution. When the cells detached, 9 ml of α-MEM medium was added to the T75 flask. The cells were counted, and 1×10^5 cells/ml were inoculated into fresh T75 flasks, followed by incubation at 37 °C in a humidified atmosphere of 95 % air and 5 % CO_2 for 24 h.

2.9.2. *Cell printing*

For the development of bioinks, MC3T3-E1 cells were encapsulated in ADA-GEL and ACP-reinforced ADA-GEL hydrogels. Cells were detached and diluted to a concentration of 2 Mio cells/ml, centrifuged at 300 g for 5 min. The supernatant was removed, and the obtained cell pellet was mixed with the respective bioinks with the help of positive displacement pipettes. Further, 2 ml of bioinks were transferred to the bioprinting cartridges, closed with a blind plug, and incubated for 10 min at 4°C. Five-layer grid structures without an outline and outer dimension of 15×15 mm^2 with maximum thickness of 1.5 mm were then printed into a six-well plate using a Cellink BioX printer equipped with a cool printhead at 23 °C. The printing speed was fixed to 5 mm/s, and 65 kPa pressure was applied. Thirty seconds after the print was completed, the constructs were crosslinked with 100 mM $CaCl_2$ and 1 % w/v microbial transglutaminase (MTG) solutions (filtered through 0.22 μm Millipore filters). Further, the samples were washed with Hanks balanced salts solution (HBSS), and α-MEM medium was added, followed by incubation at 37 °C in a humidified atmosphere of 95 % air and 5 % CO_2 for 24 h. The printability index, average pore area, and cytocompatibility analyses were performed on days 1, 3, 7, and 14.

2.10. *Post-printing analysis*

2.10.1. *Semi-quantification of printability index*

Under the ideal gelation condition of the bioink, a regular grid structure with a square-shaped pore is formed. On the other hand, when the bioink is under gelation, the extruded filament shows a liquid-like state wherein the upper layer fuses with the lower layer, creating circular pores. To analyze the pore geometry on the printed constructs, a printability index was evaluated (Jongprasitkul et al., 2022). The circularity (*C*) of an enclosed area is defined as follows:

$$C = \frac{4\pi A}{L^2} \tag{2}$$

where *L* is the perimeter, and *A* is the area of the pore. Circles have the highest circularity where *C* equals 1, whereas, for the square shape, circularity equals π/4. Therefore, previous studies have defined the bioink printability index (Pr) based on a square shape using the following function (Kyle et al., 2017):

$$\mathrm{Pr} = \frac{\pi}{4}\cdot\frac{1}{C} = \frac{L^2}{16A} \tag{3}$$

For an ideal gelation condition, the interconnected channels of the constructs would display a square shape with a Pr value of 1. Pr>1 indicates an irregular pore geometry, while Pr<1 signifies curved geometry (Ouyang, 2019). Optical images of ADA-GEL and ACP-reinforced ADA-GEL constructs were obtained using a stereo microscope. The circularity of pores (n=16) of each construct was analyzed using ImageJ software (National Institute of Health, Maryland, USA), and Pr values were calculated (Rasband, 2011). The data are presented as averages of Pr values with standard deviation.

2.10.2. *Construct stability analysis*

The printed constructs were incubated for 14 days in cell culture medium. Over time, the average pore area analysis was performed at different time points (1, 3, 7, and 14 days) to assess the conformational changes in the printed constructs. The printed constructs were visualized under a stereo microscope. The area of 16 pores was evaluated using ImageJ software. The average pore area and standard deviations were calculated and compared with the theoretical pore area of 2 mm^2 of a single pore. Initially, the average area of the pore was utilized to evaluate the effect of ACP in ADA-GEL bioink. The stability was also examined by comparing the average pore area at different time points (1, 3, 7, and 14 days).

2.10.3. *Rhodamine phalloidin/DAPI staining*

Cellular constructs were examined under an epifluorescence microscope (Axio, Carl Zeiss, Jena, Germany) to assess cell orientation. Samples (n=3) were treated with 4 % formaldehyde solution for 5 min in the dark. Subsequently, the sample was treated with 0.1 % Triton-X solution for permeation. Further, the samples were washed twice with HBSS. Afterward, the samples were stained with 5 μl/ml solution of Rhodamine-Phalloidin staining (Thermofisher Scientific, USA) for one hour, followed by 1 μl/ml DAPI (Thermofisher Scientific, USA) solution for 5 min in the dark. Further, the samples were washed, immersed in HBSS solution, and analyzed under an epifluorescence microscope.

2.10.4. *Two-Photon microscopy*

To allow for the analysis of time-based three-dimensional cell distribution and qualitative morphometry inside of the different hydrogel formulations, two-photon microscopy image XYZ stacks were recorded using an ultra-fast laser-scanning multiphoton microscope (*TriMScope II,* LaVision Biotech GmbH, Bielefeld, Germany) in conjunction with a high numerical aperture (NA = 0.95) water immersion objective, *Leica HC FLUOTAR L 25x/0.95 W VISIR* (Leica Microsystems, Wetzlar, Germany). The fluorophores (Rhodamine, DAPI) were excited at a laser wavelength of 810 nm, with a pulse frequency of 80 MHz and an exponentially increasing output power from 60 to 320 mW (first to last image plane). The backward emission signal was chromatically separated with two bandpass filters (Rhodamine: CHROMA ET 560/40x; DAPI: CHROMA ET 450/30x; Chroma, Olching, Germany) and one dichroic mirror (CHROMA T495lpxr; Chroma, Olching, Germany) before it was eventually detected by two ultrasensitive transmission photomultiplier tubes (H 7422–40 LV 5 M, Hamamatsu Photonics, Herrsching, Germany). As morphometric analysis requires relatively high resolution, the imaging parameters were set to 1024×1024 pixels with a corresponding image size of 436×436 μm and a laser scanning frequency of 800 Hz, which results in a lateral pixel size of 0.43 μm and a pixel dwell time of 0.91 μs. Given the adjusted step size in the axial direction of 2 μm, the resulting voxel size is $0.43 \times 0.43 \times 2$ μm. The height of each image stack varied according to the thickness of the printed filaments, but it ranged from approximately 300 μm to 580 μm. Therefore, each measurement yielded an image stack with 150 to 290 consecutive images. The three-dimensional image analysis and reconstruction were performed in ImageJ/FIJI (Schindelin et al., 2012).

3. Results and discussion

3.1. *Characterization of ACP*

The XRD analysis shown in Fig. 1 (A) indicates the XRD amorphous nature of the synthesized ACP (Rubenis et al., 2022). The FEG-TEM micrographs illustrated in Fig. 1 (B and C) reveal the particle size of ACP_CIT (~40 nm) and ACP_ACE (~20 nm).

The FTIR spectra of the ACP_ACE, ACP_CIT, and hydrogels are presented in Fig. 1 (D). The PO_4^{3-} group in ACP_ACE and ACP_CIT shows four different vibrations: ν_1 (950 cm^{-1}), ν_2 (400 – 470 cm^{-1}), ν_3 (1000 – 1150 cm^{-1}), and ν_4 (500 – 620 cm^{-1}) (Palencia, 2018; Rey et al., 2017). In Fig. 1 (B), the ACP_ACE and ACP_CIT show ν_1, ν_3, and ν_4 PO_4^{3-} vibrations. In ACP_CIT, the bands were observed at 1600 cm^{-1} and 1446 cm^{-1}, representing COO^- bending and COH stretching, respectively, of the carboxylic group in citrates (Tarakeshwar & Manogaran, 1994). Moreover, the peak at ~875 cm^{-1} was absent, indicating the incorporation of the COO^- group (Marković et al., 1993). Similarly, in ACP_ACE, the bands revealed at 675 cm^{-1} and 1580 cm^{-1} correspond to COO^- bending and stretching, and 1440 cm^{-1} represents COH stretching of the

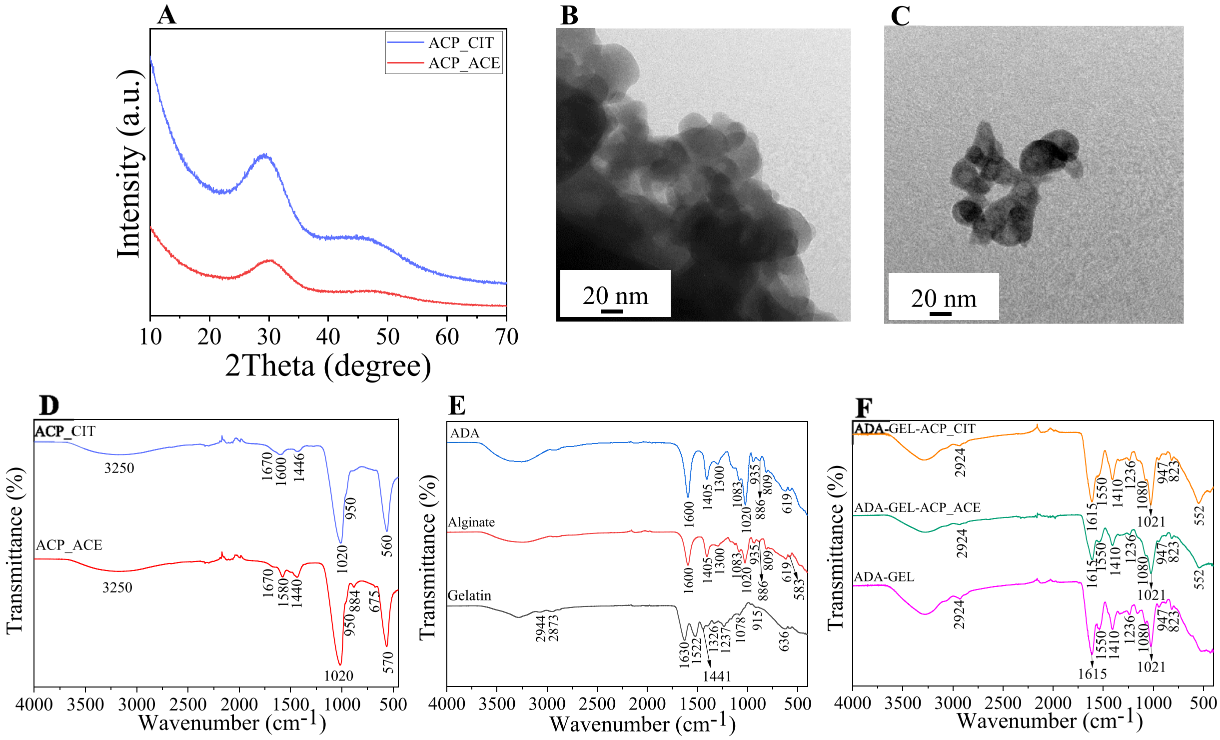

Fig. 1. Characterization of synthesized ACPs. X-Ray diffraction patterns showing amorphous ACP_ACE and ACP_CIT (A). FEG-TEM micrographs reveal the morphology and particle size of the ACP_ACE and ACP_CIT (B and C). FTIR spectra of the ACP_CIT and ACP_ACE (D) precursor materials; gelatin, sodium alginate, and alginate dialdehyde (E) and of ADA-GEL, ADA-GEL-ACP_ACE, and ADA-GEL-ACP_CIT (F).

acetate group (Safronova et al., 2017). The band observed at 884 cm^{-1} shows the HPO$_4^{2-}$ group shifting, indicating a possible association of the carboxylic group (Marković et al., 1993). The detailed characteristics such as density, solid-state ^{13}C and ^{31}P NMR, XPS, surface area, and ion release kinetics of ACP_CIT and ACP_ACE were presented in our previous article (Indurkar et al., 2023c).

In Fig. 1 (E and F), gelatin spectra show characteristic amide regions; the bands observed at wavenumbers 3310 – 3270 cm^{-1} (Amide A), 1700 – 1600 cm^{-1} (Amide I), 1550 – 1400 cm^{-1} (Amide II), and 1240 - 670 cm^{-1} (Amide III) region of gelatin (Elsayed et al., 2018). The characteristic polysaccharide structure of alginate was observed at 3300 cm^{-1} (OH stretching), 2900 cm^{-1} (-CH$_2$ stretching), 1600 cm^{-1} (O-C-O asymmetric vibrations), 1405 cm^{-1} (O-C-O symmetric vibrations and C-O-H bending), 1084 cm^{-1} (C-O and C-C vibration arising from the pyranose ring), 948 cm^{-1} (C-O vibrations from the uronic acid residue), 886 cm^{-1} and 809 cm^{-1} (in-plane bending of C1-H β-mannouronic residue) in all alginate and ADA containing samples (Husni et al., 2016).

ADA-GEL, ADA-GEL-ACP_ACE, and ADA-GEL-ACP_CIT show peaks at 1615 cm^{-1} (C=O vibrations) and 1550 cm^{-1} (C=N vibrations), confirming crosslinking by the Schiff's base formation (Indurkar al., 2020). For ADA-GEL-ACP_ACE and ADA-GEL-ACP_CIT, the v_1 and v_3 of PO$_4^{3-}$ fall within the range of ADA-GEL. Therefore, the analysis was complicated. However, the PO$_4^{3-}$ v_2 vibrations were observed at 522 cm^{-1} in ADA-GEL-ACP_CIT and ADA-GEL-ACP_ACE.

The moisture content in freshly precipitated ACP_CIT and ACP_ACE was 76.20 % and 95.9 %, respectively and the solid content in ACP_CIT and ACP_ACE precipitates was 23.80 % and 4.10 %, respectively. Based on the moisture content, 2 % (w/v) ACP was added in 5 % (w/v) ADA. Therefore, both the nanocomposite hydrogels had similar ACP concentrations. The primary reason behind the utilization of fresh precipitate rather than respective ACP powders was the metastable nature of ACP, which makes sterilization tedious (Santos et al., 2012).

3.3. *Oscillatory shear tests*

The linear viscoelastic region (LVE) of the hydrogels provides an optimum range in which the oscillatory shear tests can be performed without harming the structural properties of the hydrogel. Therefore, amplitude sweep analysis is the first step in characterizing the viscoelastic behavior of hydrogels (Indurkar, et al., 2020b). The LVE region of all the hydrogels falls within 20 % of the strain, as shown in Fig. 2 (A-C). Further analysis was performed under 1 % strain to ensure that all the measurements remained in the LVE region. While the LVE region of the hydrogels extends up to 20 % strain, selecting an amplitude closer to the upper limit of the LVE region could increase the risk of non-linear effects and/or heterogeneity in the samples. By opting for 1 % strain, a conservative approach was adopted to guarantee that the rheological properties were representative of true LVE behavior, thereby enhancing the reliability and reproducibility of the findings. Moreover, in previous studies the storage moduli (G') and loss moduli (G") of different composite bioinks were analyzed at 1 % strain during frequency sweep analysis, therefore, performing analysis at 1 % strain ensures that the data remains comparable and withing the LVE range, providing a consistent basis for comparison of results (Cidonio et al., 2019; Dubey et al., 2020; Im et al., 2022; Kim & Lin, 2021).

The frequency sweep analysis was performed to analyze the G' and G" of the hydrogels, as shown in Fig. 2 (D-F). G' represents the solid-like characteristics. At the same time, G" corresponds to the liquid-like characteristics of the hydrogel. When G'>G", the hydrogel possesses gel-like behavior, termed a viscoelastic solid, and when G'<G", the hydrogel possesses liquid-like properties, termed a viscoelastic liquid (Indurkar et al., 2020a). For bioprinting applications, the hydrogel should possess G'>G" for filament formation and shape fidelity (Kimbell & Azad, 2021). The formulated hydrogels of ADA-GEL and ACP reinforced ADA-GEL showed G'>G", favorable for bioprinting of constructs. The G' and G" values were analyzed at 1 Hz. The ADA-GEL hydrogel showed G' and G" of 99 ± 9 Pa and 9 ± 1 Pa, respectively. After addition

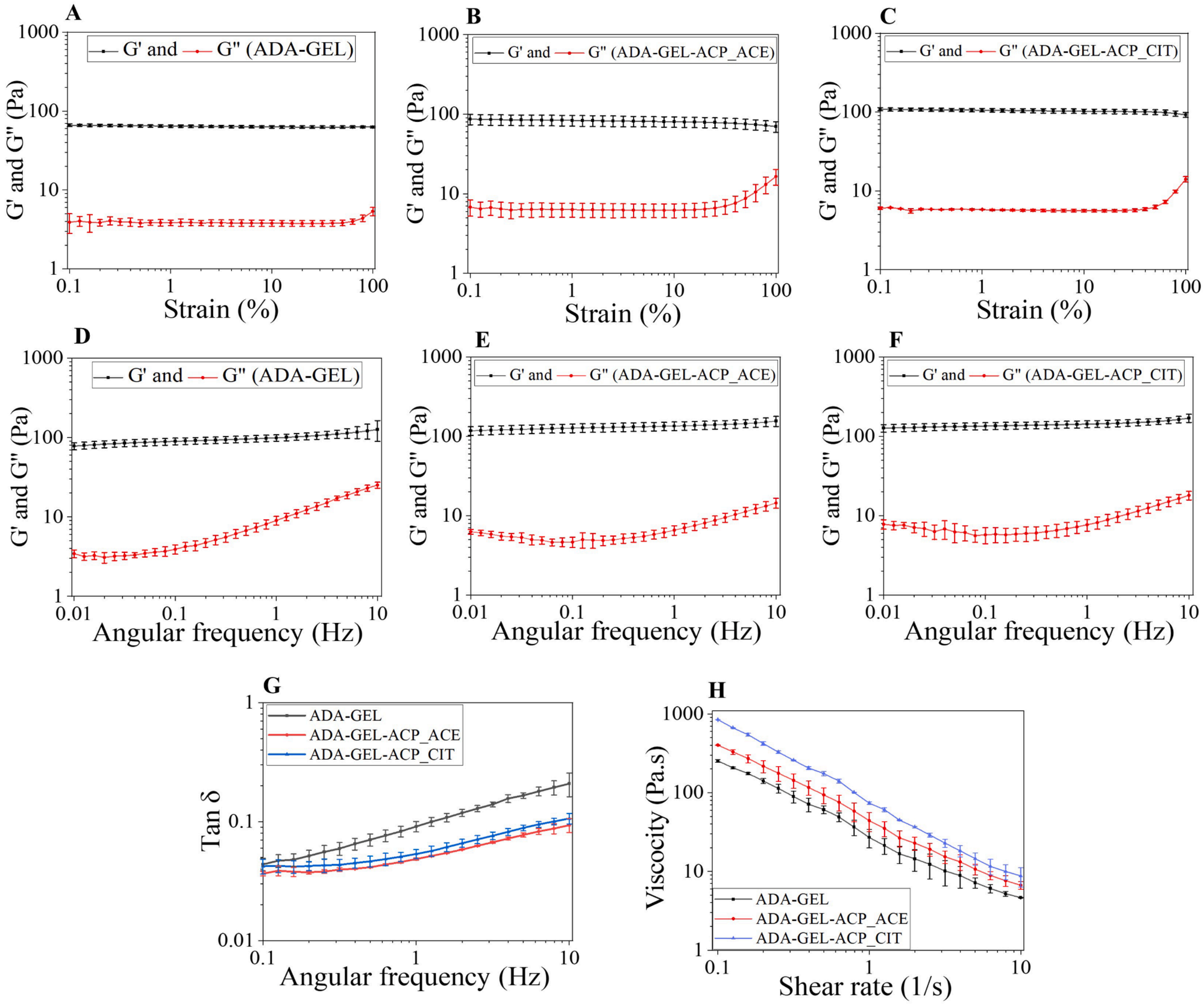

Fig. 2. Oscillatory shear tests of ADA-GEL and ACP-reinforced ADA-GEL hydrogels. Amplitude sweep analysis was performed to assess the LVE region of the hydrogel (A-C). Frequency sweep analysis to examine storage moduli (G') and loss moduli (G") of the hydrogels (D-F). Results indicate that addition of ACP in ADA-GEL enhances both G' and loss moduli G" of the ADA-GEL hydrogel. Tan δ analysis of ADA-GEL and ACP-reinforced ADA-GEL hydrogels (G). A flow behavior analysis of hydrogels was performed using viscosity analysis against shear rate. An increase in the shear rate led to decreased viscosity, revealing the shear-thinning properties of the hydrogels (H).

of ACP_ACE in ADA-GEL hydrogel, the G' and G" increased to 135 ± 16 Pa and 6.5 ± 0.5 Pa, respectively. On the other hand, with addition of ACP_CIT in ADA-GEL hydrogel, the G' and G" increased to 143 ± 14 Pa and 7.6 ± 1.2 Pa, respectively.

The tan δ analysis of all synthesized hydrogels is shown in Fig. 2 (G). Tan δ is the ratio of G" to G' of viscoelastic material, which is often used to analyze the damping properties of the material. It quantifies the ratio of energy dissipated as heat. In a viscoelastic material, a higher tan δ value (close to 1) indicates a higher proportion of energy dissipated as heat relative to the energy stored elastically. On the other hand, a lower tan δ value indicates that more energy is elastically stored compared to dissipated energy. The tan δ of ADA-GEL hydrogel was 0.09 ± 0.009. On incorporating ACP_ACE and ACP_CIT, the tan δ value of ADA-GEL hydrogel decreased to 0.048 and 0.053, respectively, indicating that incorporation of ACP enhances the elastic properties of ADA-GEL hydrogel (Hu et al., 2021).

The flow behavior of hydrogels is an essential aspect of bioprinting. A hydrogel is a Newtonian fluid if the viscosity is independent of the shear rate, but cells will experience high shear on extrusion in this case. On the other hand, if a hydrogel is a non-Newtonian shear thinning fluid, a high shear will lower the viscosity of the hydrogel, resulting in the safe extrusion of cells (Cooke & Rosenzweig, 2021). The flow behavior of all formulated hydrogels in this work possesses non-Newtonian shear thinning properties, as shown in Fig. 2 (H), and the addition of ACP did not lead to significant modification of the rheological behavior of the inks.

3.4. Compression test

To analyze the effect of the respective ACP on the mechanical properties of ADA-GEL hydrogels compression tests were carried out. The stress-strain curve in Fig. 3 (A) shows a linear increase in stress on compression. As expected, the ADA-GEL hydrogel fractured under low deformation. It failed at an average stress of 3.5 kPa at a strain of ~80 %. Meanwhile, the ACP-incorporated hydrogel fractured at higher stress; for instance, ACP_ACE failed at an average stress of 11.5 kPa at a strain of ~75 %, and ACP_CIT failed at an average stress of 12.6 kPa at a ~80 % strain. The maximum tolerated force before rupture (F_{max}) provides a direct measure of the hydrogel capacity to withstand mechanical loads before failure, which is crucial for evaluating hydrogels' robustness

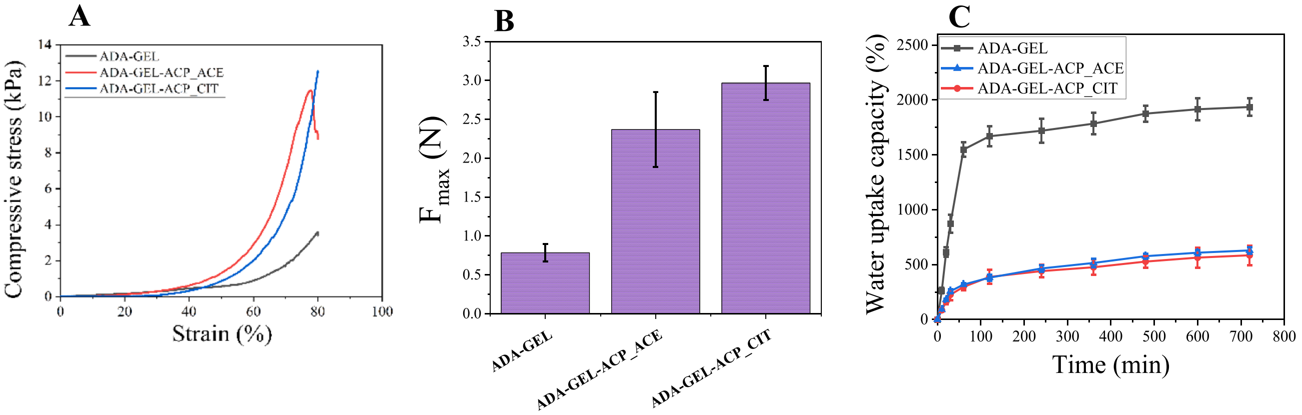

Fig. 3. Compressive stress-strain curves (A), maximum tolerated force (B), and water uptake capacity of the synthesized hydrogels (C).

(Wenger et al., 2022), as shown in Fig. 3 (B). The ADA-GEL hydrogel possesses a low F_{max} of 0.75 ± 0.11 N. The incorporation of ACP led to higher F_{max} values; for instance, ACP_ACE possesses F_{max} of 2.36 ± 0.48 N, while ACP_CIT showed F_{max} of 2.96 ± 0.22 N. Overall, incorporation of ACP led to approximately three times higher compression strength and F_{max} values, thus confirming the reinforcement of ADA_GEL hydrogel.

3.5. Water uptake capacity

Fig. 3 (C) shows the water uptake capacity of the synthesized hydrogels. The ADA-GEL hydrogel shows higher water swelling ability, which matches the result of previous studies (Sarker et al., 2014). However, incorporating ACP in the ADA-GEL hydrogel reduces its water uptake capacity. The reduction in water uptake capacity may be due to the hindrance of free polymer chain movement due to the presence of ACP (Kumar et al., 2019).

Our previous study analyzed the calcium and phosphate ion release of ACP_ACE and ACP_CIT (Indurkar et al., 2023b). The calcium ions release is critical as they can crosslink ADA (Nguyen & Lee, 2011). We postulate that the release of calcium ions shown by ACP_ACE and ACP_CIT may be responsible for the crosslinking of ADA; therefore, a reduction in water uptake capacity was observed. Moreover, the calcium ion release of ACP_CIT was higher than that of ACP_ACE, which can be attributed to the reduced water uptake capacity of ACP_CIT compared to ACP_ACE. Another mechanism that might be contributing to this effect is citrate-GEL crosslinking (Inoue et al., 2012). The free carboxyl group of citrates in ACP_CIT can potentially react with the amine group of GEL to form amide bonds. ADA, GEL, or both can be crosslinked with ACP_CIT. However, more advanced analyses are required to confirm the exact crosslinking mechanism in ACP containing hydrogels that can also contribute to reduced water uptake capacity.

3.6. Printing optimization

A trial-and-error method was performed to find the printing window of the formulated bioinks. The crosslinking step was not performed in this analysis, and the constructs were not immersed in any medium post-printing. Initially, ADA-GEL hydrogel was utilized, and the pressure was selected as a variable process parameter to keep the printing speed

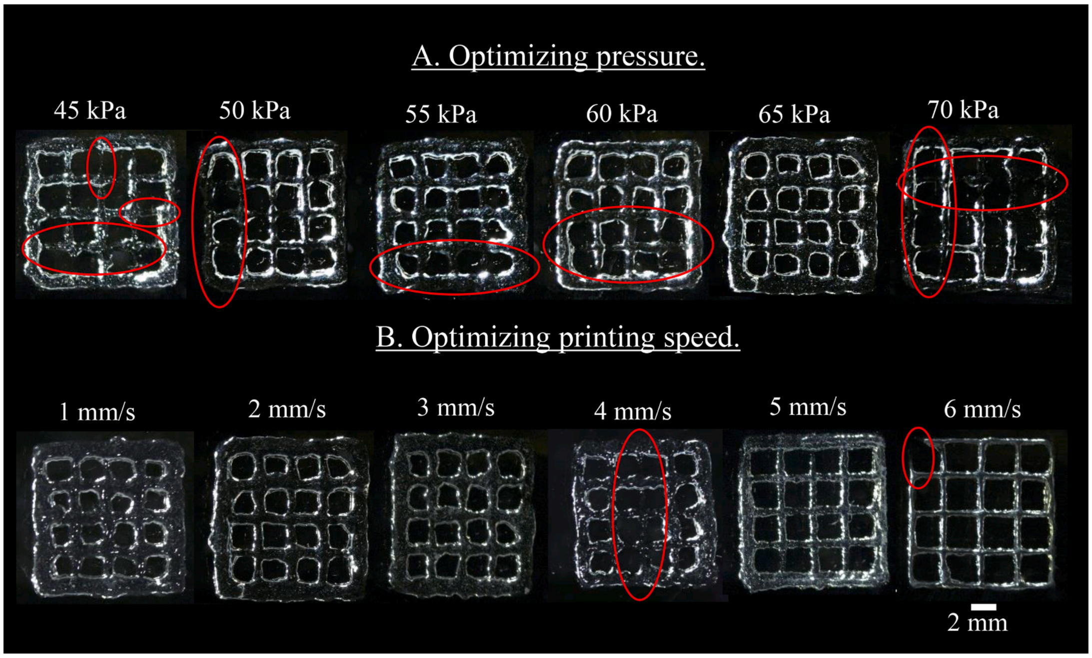

Fig. 4. Trial-and-error approach for evaluating the optimum printing outcome for ADA-GEL hydrogels under different printing pressure and speed combinations. The printing pressure was assessed initially at a slow printing speed of 2 mm/s (A). Printing was then performed at different speeds keeping the pressure at 65 kPa (B).

constant at 2 mm/sec. The printing was performed at different pressures, and the printed constructs were analyzed using stereo microscopy, as shown in Fig. 4 (A). Printing below 45 kPa did not extrude as a filament; therefore, the construct was not deemed printable. The construct was formed at a printing pressure of 45 kPa; however, there were structural inconsistencies. The gaps in the struts are shown in Fig. 4 (A) with a red ellipse. These inconsistencies in the printed structures were due to non-uniform filament formation. As the pressure increased, the inconsistencies within the construct gradually reduced. The pressure of 65 kPa formed a construct without structural inconsistency, indicating uniform filament formation. However, the construct did not display square-shaped pore geometry; therefore, printing speed optimization was performed.

In the previous step, uniform filament formation was observed when the printing pressure was 65 kPa, and the printing speed was 2 mm/s. Fig. 4 (B) shows that the printing speed optimization was performed by keeping a printing pressure of 65 kPa constant. Lowering the printing speed to 1 mm/s leads to over extrusion of the material, observed from the reduced pore size. On the contrary, increasing speed to 3 mm/s showed minor changes in the pore geometry. The geometry of pores was gradually enhanced by increasing the printing speed. A squared-shaped pore geometry was formed at a printing speed of 5 mm/s. Further, increased printing speed enhanced the pore geometry; however, structural irregularities were observed. Therefore, a printing speed of 5 mm/s and a pressure of 65 kPa were used for cell printing experiments.

3.7. Post-printing analysis

The changes in the constructs' pore geometry can be visually appreciated in Fig. 5 (A-C). On day 1, the Pr value of ADA-GEL and ACP-reinforced ADA-GEL was close to 1, indicating the square shape geometry of pores. However, in ADA-GEL bioinks, a subsequent increase in the Pr value was observed on day 3 and day 7, signifying uneven pore geometry. By day 14, the Pr value of the construct dropped below 1, indicating circular porosity. In contrast, the ACP-reinforced bioinks showed decreasing Pr values, suggesting curved porosity. Notably, compared to pristine ADA-GEL bioink, the Pr values of ACP-reinforced ADA_GEL bioinks remained relatively stable on days 3, 7, and 14.

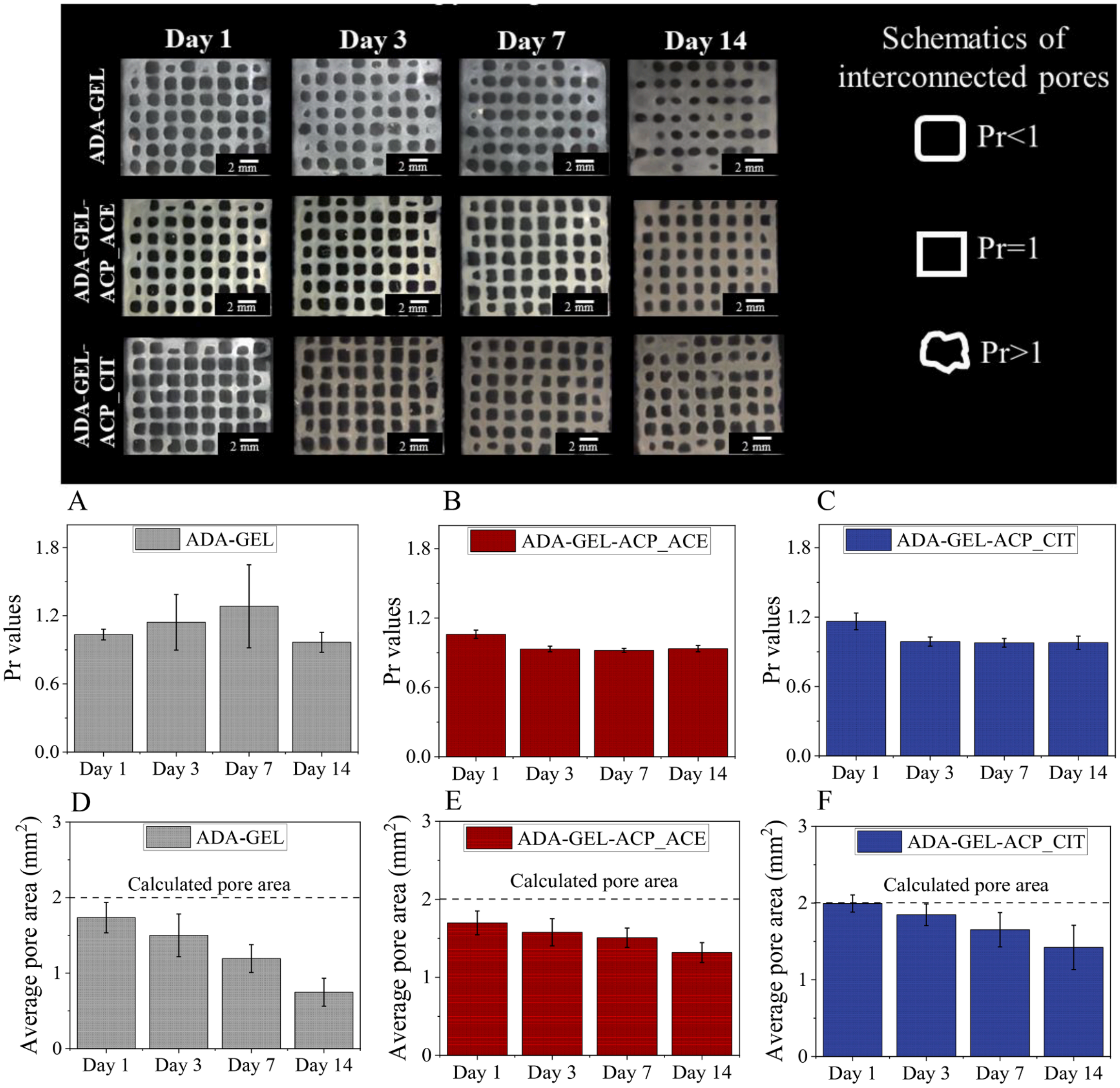

Fig. 5. Post-printing analysis of the printed constructs of ADA-GEL and ACP-reinforced ADA-GEL bioinks (ADA-GEL-ACP_ACE and ADA-GEL-ACP_CIT). Stereo microscopy image analysis was performed on days 1, 3, 7, and 14 (scale bar: 2 mm). Printability index (Pr) and average pore area analyses were performed using image J analysis by selecting 16 pores. Pore geometry was evaluated by analyzing the Pr value; for instance, Pr<1 represents curved, Pr = 1 corresponds to square, and Pr>1 resembles variable pore geometry. (A-C) Pr values and (D-F) average pore area. ADA-GEL bioinks show rapid conformational changes in pore geometry and reduced average pore area, indicating poor structural stability compared to ACP-reinforced ADA-GEL constructs.

Moreover, the construct pore area changes are presented in Fig. 5 (D-F). On day 1 the average pore area of ADA-GEL-ACP_CIT construct was close to the calculated pore area of 2 mm^2. However, the ADA-GEL-ACP_ACE and ADA-GEL constructs exhibited a reduced average pore area. Subsequently, a decrease in the average pore area was observed. In all the printed constructs after day 1, the reduction of the average pore area in ADA-GEL bioink was higher than that of ACP-reinforced ADA-GEL constructs. This analysis confirmed that ACP reinforcement in ADA-GEL hydrogel enhances the structural stability of the constructs. Notably, ACP_CIT was more effective in maintaining structural integrity than ACP_ACE.

3.8. Rhodamine phalloidin/DAPI staining

Rhodamine phalloidin staining was employed to stain F-actin (a structural and cytoskeletal protein), and DAPI was utilized to stain the nucleus of cells (Kapat et al., 2018). This staining allows for analyzing the morphology of the encapsulated MC3T3-E1 cells in the bioprinted constructs. ADA-GEL bioink was used as a positive control, and the effect of ACP_ACE and ACP_CIT on cells was analyzed. Fig. 6 shows cellular attachment on day 1, followed by cell elongation, fusion, and network formation on the consecutive days. The scaffolds were entirely covered with cells on day 14, confirming the non-cytotoxic effect of ACP_ACE and ACP_CIT in the bioinks. Magnified epifluorescence images are presented in Fig S1-S3 (in supplementary data) for enhanced visualization.

3.9. Two-photon microscopy

The cytocompatibility analysis using an inverse epifluorescence microscope revealed the cytocompatibility of the constructs. Additionally, two-photon microscopy was performed to analyze the three-dimensional cell distribution within the biofabricated constructs at depth. This technique can resolve fluorescently labeled cells within thick samples, strongly scattering samples, while reducing phototoxicity (O'rourke & Rubart, 2004). To provide a clear view of the cell distribution, the 3D reconstructions of the obtained two-photon microscopy image stacks are presented in Fig. 7. The XY images (top-down view along the optical axis) indicate homogeneous distribution on the surface of the respective hydrogels, as shown in Fig. 7 (A). On the other hand, the YZ images (the stack was rotated by 90° around the Y axis) show how cells are colonized inside the respective bioinks Fig. 7 (B). From the images, it can be concluded that the cell population gradually grows over time in the constructs, supporting the results from the epifluorescence microscopy experiments. Moreover, the cells are well embedded within the constructs, confirming the fabricated bioinks' cytocompatibility.

4. Conclusions

Incorporating ACP improved the viscoelastic and mechanical properties of ADA-GEL hydrogels. The bioinks were developed by embedding MC3T3-E1 cells into the respective hydrogels. $CaCl_2$ and MTG were used as crosslinkers to impart structural integrity. Post-printing analysis (printability index and average pore size) was performed, and the stability of the constructs was analyzed. Results revealed that ADA-GEL-ACP_CIT constructs were the most stable compared to ADA-GEL-ACP_ACE, with minimum stability observed in ADA-GEL constructs. The cellular analysis confirmed the cytocompatibility of the bioinks. Further research should investigate the printing of thicker constructs and the study of the bioink's interaction with different cell types, ultimately advancing the prospects of application of 3D printed constructs in personalized bone tissue regeneration and repair.

CRediT authorship contribution statement

Abhishek Indurkar: Writing – review & editing, Writing – original draft, Visualization, Validation, Methodology, Investigation, Formal analysis, Data curation, Conceptualization. **Susanne Heid:** Writing – review & editing, Methodology, Formal analysis, Data curation. **Julian Bauer:** Writing – review & editing, Data curation. **Kristaps Rubenis:** Writing – review & editing. **Oliver Friedrich:** Writing – review & editing, Supervision. **Janis Locs:** Writing – review & editing, Supervision, Resources, Conceptualization. **Aldo R. Boccaccini:** Writing – review & editing, Supervision, Resources, Conceptualization.

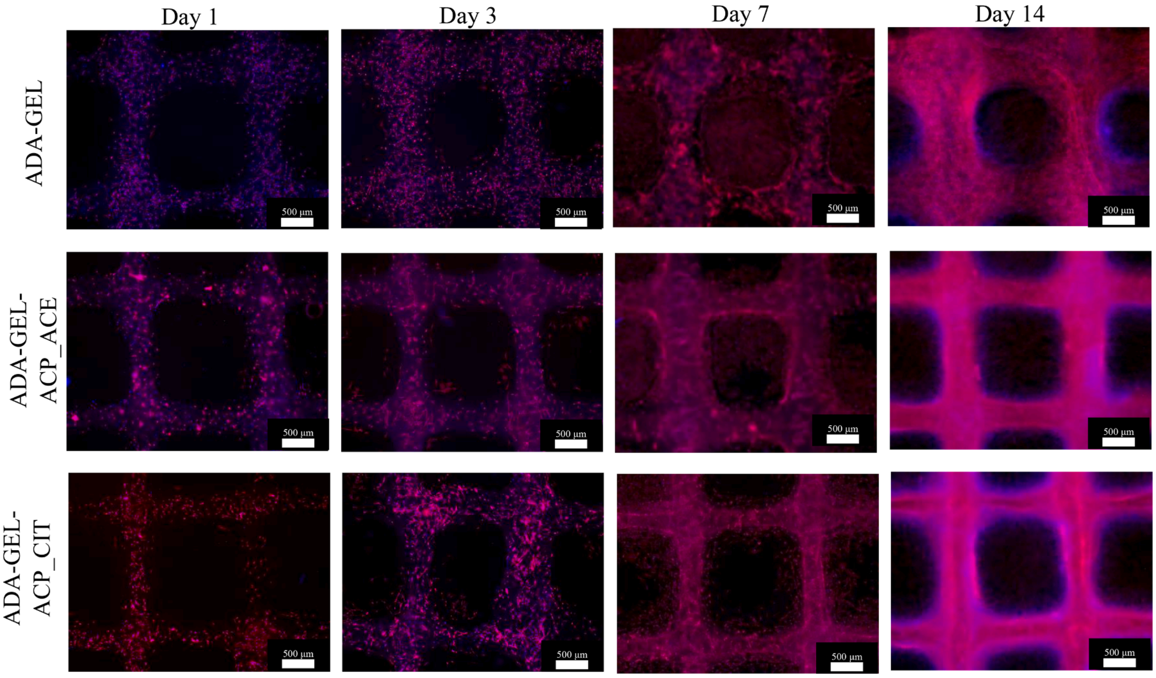

Fig. 6. Epifluorescence microscopy of rhodamine-phalloidin (red) and DAPI (blue) staining of MC3T3-E1 cells embedded in ADA-GEL and ACP reinforced ADA-GEL constructs (ADA-GEL-ACP_ACE and ADA-GEL-ACP_ACE). (Scale bar: 500 µm).

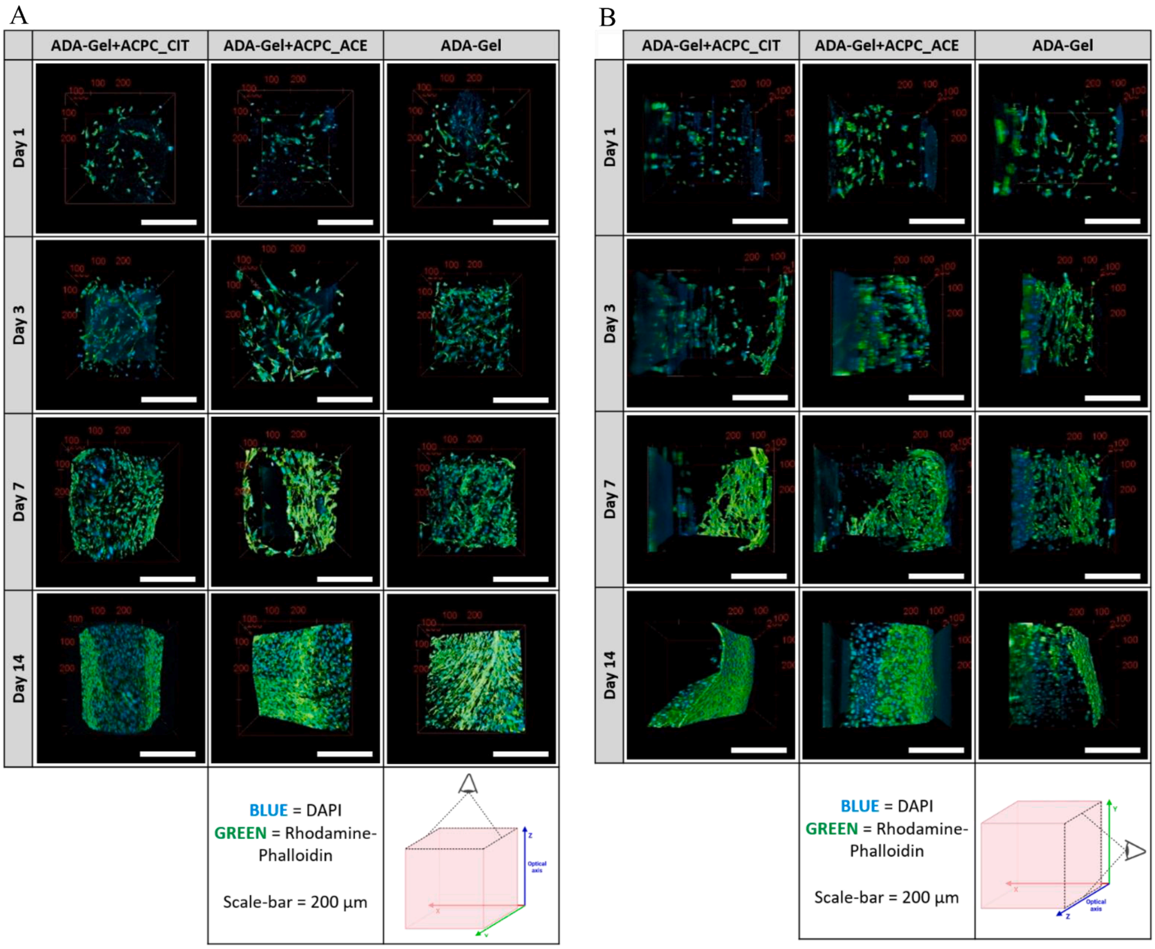

Fig. 7. Three-dimensionally reconstructed multiphoton microscopy images for qualitative morphometry and cell distribution analysis. The two different viewing angles onto three-dimensionally reconstructed multiphoton image stacks. One representative image stack was chosen for each hydrogel composition, three-dimensionally reconstructed, and single images of the transversal (XY, top-down view along the optical axis) and the sagittal (YZ, rotated by 90 °) plane were taken. While the XY perspective allows for qualitative morphometry (A), the YZ perspective provides the opportunity to qualitatively determine the homogeneity of the cell distribution inside the hydrogel filament (B). The green Lookup-Table represents actin filaments stained with Rhodamine-Phalloidin, and the blue table shows the cell nuclei stained with DAPI.

Declaration of competing interest

The authors declare that they have no known competing financial interests or personal relationships that could have appeared to influence the work reported in this paper.

Acknowledgements

The authors acknowledge financial support from the European Union's Horizon 2020 research and innovation program under grant agreement No. 857287 (BBCE) and Baltic Research Programme Project No. EEA-RESEARCH-85 "Waste-to-resource: eggshells as a source for next generation biomaterials for bone regeneration (EGGSHELL)" under the EEA Grant of Iceland, Liechtenstein and Norway No. EEZ/BPP/VIAA/2021/1. J.B., O.F., A.R.B. and S.H. were financially supported by Deutsche Forschungsgemeinschaft (DFG, German Research Foundation), Project #326998133, TRR225 Biofabrication (subproject Z02 to O.F. and subproject B03 to A.R.B.).

Data availability

The datasets generated during and/or analyzed during the current study are available from the corresponding author on reasonable request.

References

Bozo, I. Y., Deev, R. V., Smirnov, I. V., Fedotov, A. Y., Popov, V. K., Mironov, A. V., et al. (2020). 3D Printed gene-activated octacalcium phosphate implants for large bone defects engineering. *International Journal of Bioprinting, 6*(3), 93–109. https://doi.org/10.18063/IJB.V6I3.275

Buschmann, J., Härter, L., Gao, S., Hemmi, S., Welti, M., Hild, N., et al. (2012). Tissue engineered bone grafts based on biomimetic nanocomposite PLGA/amorphous calcium phosphate scaffold and human adipose-derived stem cells. *Injury, 43*(10), 1689–1697. https://doi.org/10.1016/J.INJURY.2012.06.004

Chen, F., Yang, B., Qi, C., Sun, T. W., Jiang, Y. Y., Wu, J., et al. (2015). An amorphous calcium phosphate nanocomposite for storing and sustained release of IgY protein with antibacterial activity. *RSC Advances, 5*(122), 100682–100688. https://doi.org/10.1039/C5RA19065G

Chen, S., Liu, D., Fu, L., Ni, B., Chen, Z., Knaus, J., et al. (2023). Formation of amorphous iron-calcium phosphate with high stability. *Advanced Materials.* , Article 2301422. https://doi.org/10.1002/ADMA.202301422

Chen, Y., Gu, W., Pan, H., Jiang, S., & Tang, R. (2014). Stabilizing amorphous calcium phosphate phase by citrate adsorption. *CrystEngComm, 16*(10), 1864–1867. https://doi.org/10.1039/C3CE42274G

Cheng, L., Weir, M. D., Xu, H. H. K., Antonucci, J. M., Kraigsley, A. M., Lin, N. J., et al. (2012a). Antibacterial amorphous calcium phosphate nanocomposites with a quaternary ammonium dimethacrylate and silver nanoparticles. *Dental Materials : Official Publication of the Academy of Dental Materials, 28*(5), 561–572. https://doi.org/10.1016/J.DENTAL.2012.01.005

Cheng, L., Weir, M. D., Xu, H. H. K., Antonucci, J. M., Lin, N. J., Lin-Gibson, S., et al. (2012b). Antibacterial nanocomposites containing amorphous calcium phosphate and silver nanoparticles with different filler levels. *Journal of Biomedical Materials Research - Part B Applied Biomaterials, 100*(5), 1378–1386. https://doi.org/10.1002/JBM.B.32709

Cidonio, G., Cooke, M., Glinka, M., Dawson, J. I., Grover, L., & Oreffo, R. O. C (2019). Printing bone in a gel: using nanocomposite bioink to print functionalised bone scaffolds. *Materials Today Bio, 4*, Article 100028. https://doi.org/10.1016/J.MTBIO.2019.100028

Contessi Negrini, N., Angelova Volponi, A., Higgins, C. A., Sharpe, P. T., & Celiz, A. D (2021). Scaffold-based developmental tissue engineering strategies for ectodermal organ regeneration. *Materials Today Bio, 10*, Article 100107. https://doi.org/10.1016/J.MTBIO.2021.100107

Cooke, M. E., & Rosenzweig, D. H. (2021). The rheology of direct and suspended extrusion bioprinting. *APL Bioengineering, 5*(1), 11502. https://doi.org/10.1063/5.0031475

Costello, L. C., Franklin, R. B., Reynolds, M. A., & Chellaiah, M. (2012). The important role of osteoblasts and citrate production in bone formation: "Osteoblast citration" as a new concept for an old relationship. *The Open Bone Journal, 4*(1), 27–34. https://doi.org/10.2174/1876525401204010027

Duarte Campos, D. F., Rohde, M., Ross, M., Anvari, P., Blaeser, A., Vogt, M., et al. (2019). Corneal bioprinting utilizing collagen-based bioinks and primary human keratocytes. *Journal of Biomedical Materials Research Part A, 107*(9), 1945–1953. https://doi.org/10.1002/JBM.A.36702

Dubey, N., Ferreira, J. A., Malda, J., Bhaduri, S. B., & Bottino, M. C. (2020). Extracellular matrix/amorphous magnesium phosphate bioink for 3D bioprinting of craniomaxillofacial bone tissue. *ACS Applied Materials and Interfaces, 12*(21), 23752–23763. https://doi.org/10.1021/ACSAMI.0C05311/ASSET/IMAGES/LARGE/AM0C05311_0002.JPEG

Elsayed, H. M., Attia, R. Z., Mohamed, O. A., El-Sayed, N. H., & Ibrahim, S. A. (2018). High bloom gelatin strength from white leather shavings. *Leather and Footwear Journal, 18*(4), 259–274. https://doi.org/10.24264/LFJ.18.4.2

Fukunishi, T., Shoji, T., & Shinoka, T. (2017). Nanofiber composites in vascular tissue engineering. *Nanofiber Composites for Biomedical Applications*, 455–481. https://doi.org/10.1016/B978-0-08-100173-8.00018-1

Ghorbani, F., Reiter, T., Liverani, L., Schubert, D. W., Boccaccini, A. R., & Roether, J. A. (2023). Progress on Electrospun Composite fibers incorporating bioactive glass: An overview. *Advanced Engineering Materials, 25*(6), Article 2201103. https://doi.org/10.1002/ADEM.202201103

Granchi, D., Baldini, N., Ulivieri, F. M., & Caudarella, R. (2019). Role of citrate in pathophysiology and medical management of bone diseases. *Nutrients, 11*(11). https://doi.org/10.3390/NU11112576

Heid, S., Becker, K., Byun, J., Biermann, I., Neščáková, Z., Zhu, H., et al. (2022). Bioprinting with bioactive alginate dialdehyde-gelatin (ADA-GEL) composite bioinks: Time-dependent in-situ crosslinking via addition of calcium-silicate particles tunes in vitro stability of 3D bioprinted constructs. *Bioprinting (Amsterdam, Netherlands), 26*, e00200. https://doi.org/10.1016/J.BPRINT.2022.E00200

Hou, X., Zhang, L., Zhou, Z., Luo, X., Wang, T., Zhao, X., et al. (2022). Calcium phosphate-based biomaterials for bone repair. *Journal of Functional Biomaterials, 13*(4). https://doi.org/10.3390/JFB13040187

Hu, C., Hahn, L., Yang, M., Altmann, A., Stahlhut, P., Groll, J., et al. (2021). Improving printability of a thermoresponsive hydrogel biomaterial ink by nanoclay addition. *Journal of Materials Science, 56*(1), 691–705. https://doi.org/10.1007/S10853-020-05190-5/FIGURES/6

Hu, Y. Y., Rawal, A., & Schmidt-Rohr, K. (2010). Strongly bound citrate stabilizes the apatite nanocrystals in bone. *Proceedings of the National Academy of Sciences of the United States of America, 107*(52), 22425–22429. https://doi.org/10.1073/PNAS.1009219107/ASSET/B53276B2-073E-40A7-B8F7-E28AC70040CD/ASSETS/GRAPHIC/PNAS.1009219107EQ8.GIF

Husni, A., Pawestri, S., & Isnansetyo, A. (2016). Blood glucose level and lipid profile of alloxan–induced diabetic rats treated with na-alginate from seaweed turbinaria ornata (Turner) J.agardh. *Jurnal Teknologi, 78*(4–2), 7–14. https://doi.org/10.11113/JT.V78.8145

Hwang, E. T., Tatavarty, R., Chung, J., & Gu, M. B. (2013). New functional amorphous calcium phosphate nanocomposites by enzyme-assisted biomineralization. *ACS Applied Materials and Interfaces, 5*(3), 532–537. https://doi.org/10.1021/AM302580P/ASSET/IMAGES/MEDIUM/AM-2012-02580P_0010.GIF

Im, S., Choe, G., Seok, J. M., Yeo, S. J., Lee, J. H., Kim, W. D., et al. (2022). An osteogenic bioink composed of alginate, cellulose nanofibrils, and polydopamine nanoparticles for 3D bioprinting and bone tissue engineering. *International Journal of Biological Macromolecules, 205*, 520–529. https://doi.org/10.1016/J.IJBIOMAC.2022.02.012

Indurkar, A., Bangde, P., Gore, M., Agrawal, A. K., Jain, R., & Dandekar, P. (2020a). Fabrication of guar gum-gelatin scaffold for soft tissue engineering. *Carbohydrate Polymer Technologies and Applications, 1*, Article 100006. https://doi.org/10.1016/J.CARPTA.2020.100006

Indurkar, A., Bangde, P., Gore, M., Reddy, P., Jain, R., & Dandekar, P. (2020b). Optimization of guar gum-gelatin bioink for 3D printing of mammalian cells. *Bioprinting (Amsterdam, Netherlands), 20*, e00101. https://doi.org/10.1016/J.BPRINT.2020.E00101

Indurkar, A., Choudhary, R., Rubenis, K., & Locs, J. (2023a). Role of carboxylic organic molecules in interfibrillar collagen mineralization. *Frontiers in Bioengineering and Biotechnology, 11*, 439. https://doi.org/10.3389/FBIOE.2023.1150037

Indurkar, A., Choudhary, R., Rubenis, K., Nimbalkar, M., Sarakovskis, A., Boccaccini, R., et al. (2023b). Amorphous calcium phosphate and Amorphous calcium phosphate carboxylate: Synthesis and characterization. *ACS Omega, 8*(30), 26782–26792. https://doi.org/10.1021/acsomega.3c00796

Indurkar, A., Kudale, P., Rjabovs, V., Heinmaa, I., Demir, Ö., Kirejevs, M., et al. (2023c). Small organic molecules containing amorphous calcium phosphate: Synthesis, characterization and transformation. *Frontiers in Bioengineering and Biotechnology, 11*, Article 1329752. https://doi.org/10.3389/FBIOE.2023.1329752/BIBTEX

Inoue, M., Sasaki, M., Nakasu, A., Takayanagi, M., & Taguchi, T. (2012). An antithrombogenic citric acid-crosslinked gelatin with endothelialization activity. *Advanced Healthcare Materials, 1*(5), 573–581. https://doi.org/10.1002/ADHM.201200001

Jeong, J., Kim, J. H., Shim, J. H., Hwang, N. S., & Heo, C. Y. (2019). Bioactive calcium phosphate materials and applications in bone regeneration. *Biomaterials Research, 23*(1), 1–11. https://doi.org/10.1186/S40824-018-0149-3. *2019 23:1*.

Jiang, Y., Tan, S., Hu, J., Chen, X., Chen, F., Yao, Q., et al. (2021). Amorphous calcium magnesium phosphate nanocomposites with superior osteogenic activity for bone regeneration. *Regenerative Biomaterials, 8*(6), 1–11. https://doi.org/10.1093/RB/RBAB068

Jin, W., Liu, Z., Wu, Y., Jin, B., Shao, C., Xu, X., et al. (2018). Synergic effect of Sr2+ and Mg2+ on the stabilization of amorphous calcium phosphate. *Crystal Growth & Design, 18*(10), 6054–6060. https://doi.org/10.1021/ACS.CGD.8B00908

Jongprasitkul, H., Turunen, S., Parihar, V. S., & Kellomäki, M. (2022). Two-step crosslinking to enhance the printability of methacrylated gellan gum biomaterial ink for extrusion-based 3D bioprinting. *Bioprinting (Amsterdam, Netherlands), 25*. https://doi.org/10.1016/J.BPRINT.2021.E00185

Joseph, B., Jose, C., Kavil, S. V., Kalarikkal, N., & Thomas, S. (2023). Solvent-casting approach for design of polymer scaffolds and their multifunctional applications. *Functional Biomaterials: Design and Development for Biotechnology, Pharmacology, and Biomedicine*, 371–394. https://doi.org/10.1002/9783527827657.CH12. *2 Volumes*.

Kapat, K., Maity, P. P., Rameshbabu, A. P., Srivas, P. K., Majumdar, P., & Dhara, S. (2018). Simultaneous hydrothermal bioactivation with nano-topographic modulation of porous titanium alloys towards enhanced osteogenic and antimicrobial responses. *Journal of Materials Chemistry B, 6*(18), 2877–2893. https://doi.org/10.1039/C8TB00382C

Kim, D., Lee, J. U., & Kim, G. H. (2020). Biomimetic gelatin/HA biocomposites with effective elastic properties and 3D-structural flexibility using a 3D-printing process. *Additive Manufacturing, 36*, Article 101616. https://doi.org/10.1016/J.ADDMA.2020.101616

Kim, M. H., & Lin, C. C. (2021). Norbornene-functionalized methylcellulose as a thermo- and photo-responsive bioink. *Biofabrication, 13*(4), Article 045023. https://doi.org/10.1088/1758-5090/AC24DC

Kimbell, G., & Azad, M. A. (2021). 3D printing: Bioinspired materials for drug delivery. *Bioinspired and Biomimetic Materials for Drug Delivery*, 295–318. https://doi.org/10.1016/B978-0-12-821352-0.00011-3

Krogstad, D., Wang, D., & Lin-Gibson, S. (2014). The role of polyelectrolytes in the stabilization of calcium phosphate nanoparticles for the production of biomimetic materials. *APS, 2014*. W11.009 https://ui.adsabs.harvard.edu/abs/2014APS..MARW11009K/abstract.

Kumar, B. Y. S., Isloor, A. M., Kumar, G. C. M., Inamuddin, & Asiri, A. M (2019). Nanohydroxyapatite reinforced Chitosan composite hydrogel with tunable mechanical and biological properties for cartilage regeneration. *Scientific Reports, 9*(1), 1–13. https://doi.org/10.1038/s41598-019-52042-7. *2019 9:1*.

Kundu, J., Pati, F., Shim, J. H., & Cho, D. W. (2014). Rapid prototyping technology for bone regeneration. *Rapid Prototyping of Biomaterials: Principles and Applications*, 254–284. https://doi.org/10.1533/9780857097217.254

Kyle, S., Jessop, Z. M., Al-Sabah, A., & Whitaker, I. S. (2017). Printability'' of candidate biomaterials for extrusion based 3D printing: State-of-the-art. *Advanced Healthcare Materials, 6*(16). https://doi.org/10.1002/ADHM.201700264

Łabowska, M. B., Cierluk, K., Jankowska, A. M., Kulbacka, J., Detyna, J., & Michalak, I. (2021). A review on the adaption of alginate-gelatin hydrogels for 3D cultures and bioprinting. *Materials, 14*(4), 1–28. https://doi.org/10.3390/MA14040858

Lehninger, A. L. (1970). Mitochondria and calcium ion transport the fifth jubilee lecture. *The Biochemical Journal, 119*(2), 129–138.

Li, N., Guo, R., & Zhang, Z. J. (2021). Bioink formulations for bone tissue regeneration. *Frontiers in Bioengineering and Biotechnology, 9*, Article 630488. https://doi.org/10.3389/FBIOE.2021.630488/BIBTEX

Liu, H., Xing, F., Yu, P., Zhe, M., Shakya, S., Liu, M., et al. (2024). Multifunctional aerogel: A unique and advanced biomaterial for tissue regeneration and repair. *Materials & Design, 243*, Article 113091. https://doi.org/10.1016/J.MATDES.2024.113091

Liu, Y., Li, N., Qi, Y. P., Dai, L., Bryan, T. E., Mao, J., et al. (2011). Intrafibrillar collagen mineralization produced by biomimetic hierarchical nanoapatite assembly. *Advanced Materials (Deerfield Beach, Fla.), 23*(8), 975. https://doi.org/10.1002/ADMA.201003882

Mao, H., Yang, L., Zhu, H., Wu, L., Ji, P., Yang, J., et al. (2020). Recent advances and challenges in materials for 3D bioprinting. *Progress in Natural Science: Materials International, 30*(5), 618–634. https://doi.org/10.1016/J.PNSC.2020.09.015

Marković, M., Brown, W. E., & Fowler, B. O. (1993). Octacalcium phosphate carboxylates. 2. Characterization and structural considerations. *Chemistry of Materials, 5*(10), 1406–1416. https://doi.org/10.1021/CM00034A008

Nguyen, T.P., & Lee, B.T. (2011). Fabrication of oxidized alginate-gelatin-BCP hydrogels and evaluation of the microstructure, material properties and biocompatibility for bone tissue regeneration, 27(3), 311–321. https://doi.org/10.1177/0885328211404265.

Niu, X., Liu, Z., Tian, F., Chen, S., Lei, L., Jiang, T., et al. (2017). Sustained delivery of calcium and orthophosphate ions from amorphous calcium phosphate and poly(L-lactic acid)-based electrospinning nanofibrous scaffold. *Scientific Reports, 7*(1), 1–9. https://doi.org/10.1038/srep45655. *2017 7:1*.

Nudelman, F., Lausch, A. J., Sommerdijk, N. A. J. M., & Sone, E. D. (2013). In vitro models of collagen biomineralization. *Journal of Structural Biology, 183*(2), 258–269. https://doi.org/10.1016/J.JSB.2013.04.003

O'rourke, B., & Rubart, M. (2004). Two-photon microscopy of cells and tissue. *Circulation Research, 95*(12), 1154–1166. https://doi.org/10.1161/01.RES.0000150593.30324.42

Ouyang, L. (2019). 3D bioprinting of thermal-sensitive bioink, in: Study on Microextrusion-based 3D Bioprinting and Bioink. *Crosslinking Mechanisms, Springer Theses* (pp. 63–80). Singapore: Springer. https://doi.org/10.1007/978-981-13-9455-3_5

Palencia, M. (2018). Functional transformation of fourier-transform mid-infrared spectrum for improving spectral specificity by simple algorithm based on wavelet-like functions. *Journal of Advanced Research, 14*, 53–62. https://doi.org/10.1016/J.JARE.2018.05.009

Rasband, W. (2011). *ImageJ, U.S. national institutes of health*. USA: Bethesda, Maryland.

Rehm, B., & Haghshenas, A. (2012). Flow drilling: Underbalance drilling with liquid single-phase systems. *Underbalanced Drilling: Limits and Extremes*, 39–108. https://doi.org/10.1016/B978-1-933762-05-0.50009-7

Rey, C., Combes, C., Drouet, C., Grossin, D., Bertrand, G., & Soulié, J. (2017). 1.11 Bioactive calcium phosphate compounds: Physical chemistry. *Comprehensive Biomaterials, II*, 244–290. https://doi.org/10.1016/B978-0-12-803581-8.10171-7

Rubenis, K., Zemjane, S., Vecstaudza, J., Lazdovica, K., Bitenieks, J., Wiecinski, P., et al. (2022). Sintering of amorphous calcium phosphate to near-full density by uniaxial compaction at room temperature. *Journal of the European Ceramic Society, 42*(13), 6199–6205. https://doi.org/10.1016/J.JEURCERAMSOC.2022.06.041

Safronova, T. V., Mukhin, E. A., Putlyaev, V. I., Knotko, A. V., Evdokimov, P. V., Shatalova, T. B., et al. (2017). Amorphous calcium phosphate powder synthesized from calcium acetate and polyphosphoric acid for bioceramics application. *Ceramics International, 43*(1), 1310–1317. https://doi.org/10.1016/J.CERAMINT.2016.10.085

Santos, C., Gomes, P. S., Duarte, J. A., Franke, R. P., Almeida, M. M., Costa, M. E. V., et al. (2012). Relevance of the sterilization-induced effects on the properties of different hydroxyapatite nanoparticles and assessment of the osteoblastic cell response. *Journal of the Royal Society Interface, 9*(77), 3397. https://doi.org/10.1098/RSIF.2012.0487

Sarker, B., Singh, R., Silva, R., Roether, J. A., Kaschta, J., Detsch, R., et al. (2014). Evaluation of fibroblasts adhesion and proliferation on alginate-gelatin crosslinked hydrogel. *PloS One, 9*(9). https://doi.org/10.1371/JOURNAL.PONE.0107952

Sarker, B., Zehnder, T., Rath, S. N., Horch, R. E., Kneser, U., Detsch, R., et al. (2017). Oxidized alginate-gelatin hydrogel: A favorable matrix for growth and osteogenic differentiation of adipose-derived stem cells in 3D. *ACS Biomaterials Science and Engineering, 3*(8), 1730–1737. https://doi.org/10.1021/ACSBIOMATERIALS.7B00188/ASSET/IMAGES/MEDIUM/AB-2017-00188S_0007.GIF

Schindelin, J., Arganda-Carreras, I., Frise, E., Kaynig, V., Longair, M., Pietzsch, T., et al. (2012). Fiji: An open-source platform for biological-image analysis. *Nature Methods, 9*(7), 676–682. https://doi.org/10.1038/nmeth.2019. *2012 9:7*.

Schweikle, M., Bjørnøy, S. H., van Helvoort, A. T. J., Haugen, H. J., Sikorski, P., & Tiainen, H. (2019a). Stabilisation of amorphous calcium phosphate in polyethylene glycol hydrogels. *Acta Biomaterialia, 90*, 132–145. https://doi.org/10.1016/J.ACTBIO.2019.03.044

Schweikle, M., Bjørnøy, S. H., van Helvoort, A. T. J., Haugen, H. J., Sikorski, P., & Tiainen, H. (2019b). Stabilisation of amorphous calcium phosphate in polyethylene glycol hydrogels. *Acta Biomaterialia, 90*, 132–145. https://doi.org/10.1016/J.ACTBIO.2019.03.044

Shao, C., Zhao, R., Jiang, S., Yao, S., Wu, Z., Jin, B., et al. (2018). Citrate improves collagen mineralization via interface wetting: A physicochemical understanding of biomineralization control. *Advanced Materials (Deerfield Beach, Fla.), 30*(8). https://doi.org/10.1002/ADMA.201704876

Suamte, L., Tirkey, A., Barman, J., & Jayasekhar Babu, P. (2023). Various manufacturing methods and ideal properties of scaffolds for tissue engineering applications. *Smart Materials in Manufacturing, 1*, Article 100011. https://doi.org/10.1016/J.SMMF.2022.100011

Sun, R., Åhlén, M., Tai, C. W., Bajnóczi, É. G., de Kleijne, F., Ferraz, N., et al. (2019). Highly porous amorphous calcium phosphate for drug delivery and bio-medical applications. *Nanomaterials, 10*(1), 20. https://doi.org/10.3390/NANO10010020. *2020, Vol. 10, Page 20*.

Tarakeshwar, P., & Manogaran, S. (1994). Ground state vibrations of citric acid and the citrate trianion—An ab initio study. *Spectrochimica Acta Part A: Molecular Spectroscopy, 50*(14), 2327–2343. https://doi.org/10.1016/0584-8539(94)E0017-5

Vanaei, S., Parizi, M. S., Vanaei, S., Salemizadehparizi, F., & Vanaei, H. R. (2021). An overview on materials and techniques in 3D bioprinting toward biomedical application. *Engineered Regeneration, 2*, 1–18. https://doi.org/10.1016/J.ENGREG.2020.12.001

Weir, M.D., Chow, L.C., & Xu, H.H.K. (2012). Remineralization of demineralized enamel via calcium phosphate nanocomposite. 91(10), 979–984. https://doi.org/10.1177/0022034512458288.

Wenger, L., Radtke, C. P., Gerisch, E., Kollmann, M., Niemeyer, C. M., Rabe, K. S., et al. (2022). Systematic evaluation of agarose- and agar-based bioinks for extrusion-based bioprinting of enzymatically active hydrogels. *Frontiers in Bioengineering and Biotechnology, 10*, Article 928878. https://doi.org/10.3389/FBIOE.2022.928878/FULL

Williams, N. C., & O'Neill, L. A. J (2018). A role for the Krebs cycle intermediate citrate in metabolic reprogramming in innate immunity and inflammation. *Frontiers in Immunology, 9*(FEB), 1. https://doi.org/10.3389/FIMMU.2018.00141

Wolint, P., Näf, L., Schibler, D., Hild, N., Stark, W. J., Giovanoli, P., et al. (2021). Suspension of amorphous calcium phosphate nanoparticles impact commitment of human adipose-derived stem cells in vitro. *Biology, 10*(7), 675. https://doi.org/10.3390/BIOLOGY10070675/S1

Wu, Y., Wenger, A., Golzar, H., & Tang, X (2020). 3D bioprinting of bicellular liver lobule-mimetic structures via microextrusion of cellulose nanocrystal-incorporated shear-thinning bioink. *Scientific Reports, 10*(1), 1–12. https://doi.org/10.1038/s41598-020-77146-3. *2020 10:1*.

Xie, B., & Nancollas, G. H. (2010). How to control the size and morphology of apatite nanocrystals in bone. *Proceedings of the National Academy of Sciences of the United States of America, 107*(52), 22369. https://doi.org/10.1073/PNAS.1017493108

Xu, H. H. K., Moreau, J. L., Sun, L., & Chow, L. C. (2011). Nanocomposite containing amorphous calcium phosphate nanoparticles for caries inhibition. *Dental Materials : Official Publication of the Academy of Dental Materials, 27*(8), 762–769. https://doi.org/10.1016/J.DENTAL.2011.03.016

Yu, L., & Wei, M. (2021). Biomineralization of collagen-based materials for hard tissue repair. *International Journal of Molecular Sciences, 22*(2), 1–17. https://doi.org/10.3390/IJMS22020944

Zhu, L., Luo, D., & Liu, Y. (2020). Effect of the nano/microscale structure of biomaterial scaffolds on bone regeneration. *International Journal of Oral Science, 12*(1), 1–15. https://doi.org/10.1038/s41368-020-0073-y. *2020 12:1*.